

## Multi-temporal trajectory of the urban heat island centroid in Beijing, China based on a Gaussian volume model

Jinling Quan <sup>a</sup>, Yunhao Chen <sup>a,\*</sup>, Wenfeng Zhan <sup>a,b</sup>, Jinfei Wang <sup>a,c</sup>, James Voogt <sup>c</sup>, Mengjie Wang <sup>a</sup>

<sup>a</sup> State Key Laboratory of Earth Surface Processes and Resource Ecology, College of Resources Science and Technology, Beijing Normal University, Beijing 100875, China

<sup>b</sup> Jiangsu Provincial Key Laboratory of Geographic Information Science and Technology, International Institute for Earth System Science, Nanjing University, Nanjing, Jiangsu 210093, China

<sup>c</sup> Department of Geography, University of Western Ontario, London, ON N6A 5C2, Canada



### ARTICLE INFO

#### Article history:

Received 14 November 2013

Received in revised form 17 March 2014

Accepted 31 March 2014

Available online 25 April 2014

#### Keywords:

Urban heat island

Thermal remote sensing

Land surface temperature

Gaussian volume model

Centroid

Multi-temporal scale

### ABSTRACT

The trajectory of the urban heat island (UHI) centroid in three dimensions indicates the overall variation of the intensity and distribution of the UHI. This study applied the Gaussian volume model on the daily MODIS/LST products from 2000 to 2012 to derive the UHI centroid in Beijing on a multi-temporal scale. The trajectories indicated that (1) on a diurnal scale during July–September, the daytime and nighttime centroids of the UHI were primarily located in the Xicheng district near the city center, and the mean intensity was from 2.12 to 2.97 °C. The daytime centroid was in the south of the nighttime centroid and demonstrated a higher intensity and a larger core area, where Aqua obtains a higher intensity than Terra. The movement of the UHI centroid was also more significant in the north–south direction than in the east–west direction; (2) on a monthly scale, the daytime centroid moved from the northeast to the southwest by (1.85, 2.91) km from July to September, and the intensity varied from 2.16 °C (September) to 3.09 °C (August), while the nighttime centroid generally moved anticlockwise from January to December, and the intensity varied from 1.98 °C (July) to 3.07 °C (January); and (3) on an annual scale, the daytime UHI centroid in August and the nighttime UHI centroid moved toward the northeast by (2.15, 1.31) km and (0.43, 0.89) km, respectively. There was a dramatic change in the UHI prior to 2008, which was most likely caused by the numerous preparation projects for the 2008 Beijing Olympic Games. Correlation analysis demonstrated that the hot and medium-hot landscapes exhibited positive contributions to the variation of the horizontal location of UHI centroid, and NDVI and albedo showed positive contributions to the variations of daytime (less than 10%) and nighttime (close to 50%) UHI centroids, respectively. Also, we discussed the relationship between Z-dimension of UHI centroid and other UHI indicators, and the impact of missing data. This study presents scientific insights for urban planning and management in Beijing and motivates the investigation of comprehensive changes in UHI of other metropolises worldwide.

© 2014 Elsevier Inc. All rights reserved.

### 1. Introduction

With rapid urbanization, the land surface and atmospheric condition are modified, resulting in higher urban temperatures compared to simultaneous temperatures of the surrounding rural areas, which is known as the urban heat island (UHI) effect. This phenomenon is of great significance to the social, economic and environmental issues, such as human health (Patz, Campbell-Lendrum, Holloway, & Foley, 2005), energy consumption (Konopacki & Akbari, 2002), air pollution and climate change (Voogt & Oke, 2003). Numerous cities worldwide have been dramatically suffering from the UHI effect (Stewart, 2011),

which is predicted to get worse in the near future (Rizwan, Dennis, & Liu, 2008).

With the advantages of wide coverage, good temporal synchronization and various data sources, and with the improvements in data quality, remote sensing has become a powerful tool for the investigation of UHI (referring to surface urban heat island (SUHI)) in recent decades. There have been substantial advances in this research area. Reviews of SUHI are available from Roth, Oke, and Emery (1989), Gallo, Tarpley, McNab, and Karl (1995), Voogt and Oke (2003), Weng and Quattrochi (2006), and Rizwan et al. (2008).

The temporal variation of UHI is one of the most important themes in UHI studies. Many previous studies used a direct comparison of thermal images for visual interpretation, while many others used indicators to quantify the variation, such as using the difference between urban and rural mean temperatures, magnitude, extent or thermodynamic landscape index (Chen, Shi, & Li, 2002; Imhoff, Zhang, Wolfe, & Bounoua, 2010; Streutker, 2003; Tran, Uchihama, Ochi, & Yasuoka, 2006; Zhou, Chen, Wang, & Zhan, 2011). Nevertheless, most of these

\* Corresponding author at: No. 19 Xinjiekouwai Street, Beijing 100875, China. Tel./fax: +86 10 58806098.

E-mail addresses: JLQuan0123@gmail.com (J. Quan), cyh@bnu.edu.cn (Y. Chen), zhanwenfeng@foxmail.com (W. Zhan), jfwang@uwo.ca (J. Wang), javoogt@uwo.ca (J. Voogt), mjwang@mail.bnu.edu.cn (M. Wang).

indicators characterize UHI from a single perspective (Schwarz, Lautenbach, & Seppelt, 2011). "Centroid," on the other hand, is a comprehensive response to the urban thermal distribution feature. It indicates a spatial balance point of the UHI. Its neighborhood is most likely the most vulnerable zone to the strong UHI during hot and wet summers, and its trajectory reflects the overall variation in thermal intensity and distribution.

Several methods are available to derive the UHI centroid, such as isotherm, nonlinear parametric (Streutker, 2002), non-parametric fast Fourier transformation (Rajasekar & Weng, 2009), mean-standard

deviation (Wang, Chen, & Yan, 2009), geometric (Sun, Wu, & Tan, 2010) and spatial association (Xie, Fu, & Wang, 2011) methods. However, there remains at least one of the three following problems in previous studies. First, these methods use a discrete level of analysis, which ignores the spatially continual tendency of UHI and fails to describe the overall intensity of the UHI properly. Second, the source data used are temporally discrete with long time intervals, in which the results are more dependent on the selection of the source data. Finally, the multi-temporal scale variation of the UHI centroid has not been fully explored.

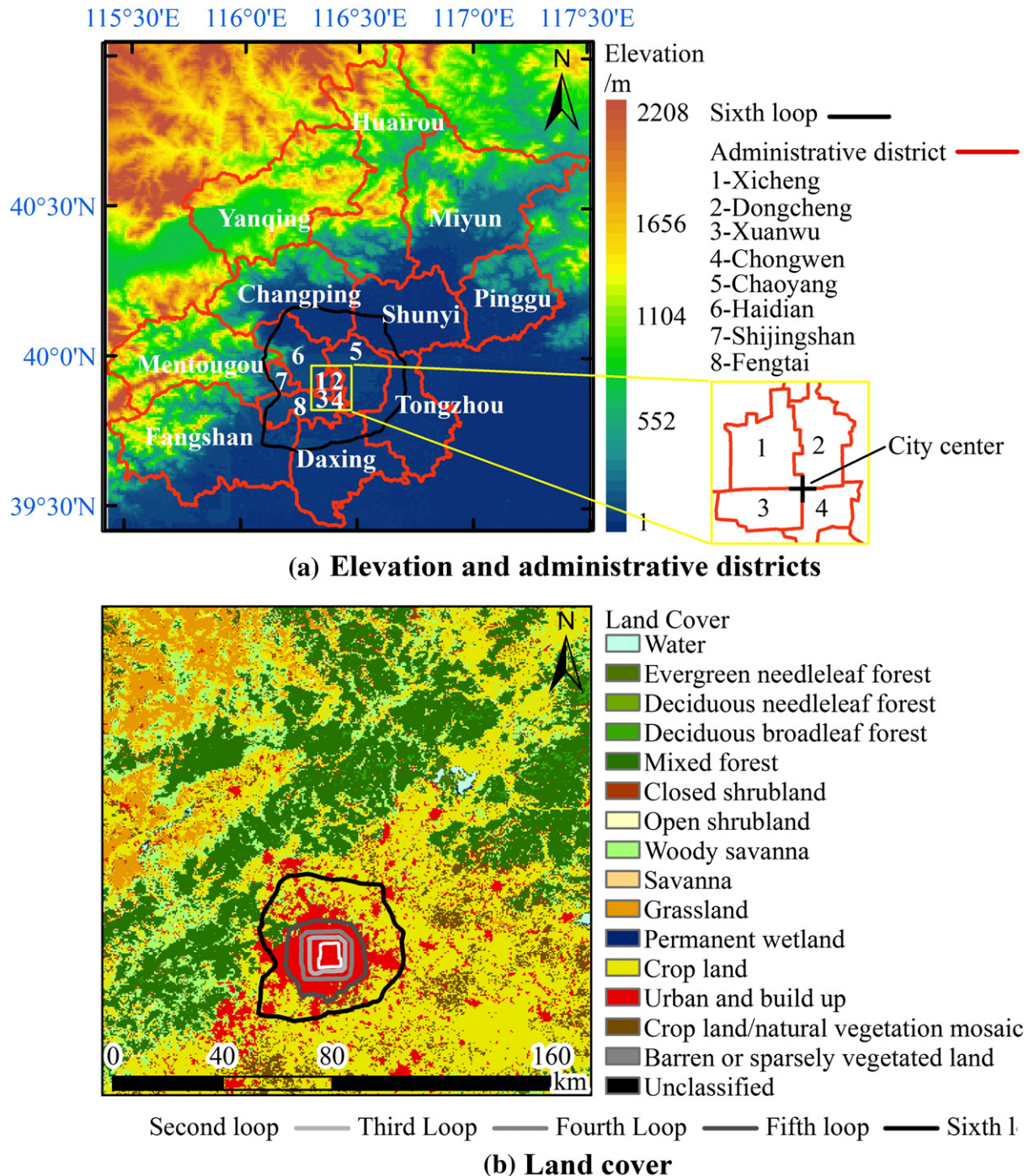


**Fig. 1.** Study area. (a) Map of the elevation and administrative districts. The intersection of districts 1–4 is defined as the city center. (b) Land cover map (Type 1) from the MODIS yearly land cover product (MCD12Q1) acquired in 2009. The administrative district boundaries and the city center are used as a background and a position reference in the following figures of the trajectories of UHI centroid.

In this research, we apply a Gaussian volume model (Zhou et al., 2011) to derive the centroid of the UHI in Beijing based on daily MODIS/LST products from 2000 to 2012. Our aim is to quantitatively detect the general variation of UHI in Beijing from a multi-temporal scale perspective. Moreover, the relationship of the horizontal location of UHI centroid with the thermal landscape and land surface characteristics, the relationship between the Z-dimension of UHI centroid and other indicators, and the impact of missing data are discussed.

## 2. Study area

We performed our analyses in Beijing, capital city of China (Fig. 1). Beijing is located between 39°28' N and 41°05' N, 115°25' E and 117°30' E. With mountains surrounding the area in the west and north, and with plains located in the east and south, Beijing exhibits a high northwestern, but low southeastern terrain (Zhan, Chen, Zhou, & Li, 2011). Temperate continental monsoon climate in Beijing causes hot and wet summers, but cold and dry winters (Zhou, Chen, Li, Weng, & Yi, 2008). Beijing has 18 administrative districts and the main transportation network is in the form of five loops from the second to the sixth loop. The land cover map (Fig. 1b) shows that the urban and built-up areas are primarily located within the sixth loop, covering districts 1–8 in Fig. 1a, which are regarded as the urban area, while croplands, that mainly cover Fangshan, Daxing, Tongzhou, Shunyi, Changping and Mentougou suburbs, are regarded as the rural area.

Beijing has undergone a period of significant urban growth with a concentric pattern in recent decades (He, Chen, Shi, & Fan, 2003). The construction area and population were approximately 3908.4 km<sup>2</sup> and 19.619 million in 2010, which is 261.5% and 80.7% larger than those in 1990, respectively (cited from the 2011 statistical yearbook of Beijing, 2011), and the difference between urban and rural air temperatures rose by 0.62 °C from 1961 to 2000 (Song & Zhang, 2003). Previous studies have indicated that Beijing has been experiencing a serious UHI (Wang & Hu, 2006; Wang, Wang, & Wang, 2007; Zhang, Hou, Li, Yan, & Yang, 2005), which induces a series of problems, such as the extreme climate, air pollution and urban wet/dry island. Therefore, investigating the general variation of UHI in the past decade is of great significance for the residential comfort and the sustainable urban development in Beijing.

## 3. Data collection and preprocessing

### 3.1. Land surface temperature (LST) data

To characterize the UHI, daily MODIS/LST products with a spatial resolution of 1 km (Terra/MOD11A1 from 2000 to 2012 and Aqua/MYD11A1 from 2002 to 2012) were utilized. The Terra and Aqua satellites were launched into near-polar sun-synchronous orbits in 1999 and 2002, respectively, and they pass in view of any point on the earth twice a day in most cases. However, the overpass time is not constant (Hu, Brunsell, Monaghan, Barlage, & Wilhelmi, 2014). The average overpass times over the urban and suburban areas in Beijing during 2000–2012 are at approximately 11:00 (ranging from 10:00 to 13:42) and 22:00 (ranging from 21:06 to 23:12), 13:00 (ranging from 12:06 to 14:06) and 02:00 (ranging from 00:06 to 03:06) at local solar time, respectively. This might induce some biases in the long time series analysis (Hu et al., 2014).

The MODIS/LST is retrieved using a generalized split-window algorithm, which corrects for atmospheric effects (including absorption and emission) and surface emissivity (Wan & Dozier, 1996), and results in an error of less than 1.0 °C in most cases (Wan, Zhang, Zhang, & Li, 2002). Because the surface UHI describes the difference between the urban and rural LSTs, the retrieval error can be partially removed in the differencing procedure. However, pixels severely contaminated by clouds or heavy aerosols have significantly higher errors (Wan, 2008).

### 3.2. Normalized difference vegetation index (NDVI) and albedo data

To interpret the movement of the UHI centroid, monthly composite MODIS/NDVI products (Terra/MOD13A3 from 2000 to 2012 and Aqua/MYD13A3 from 2002 to 2012) and 16-day Terra/Aqua composite albedo products (MCD43B3 from 2000 to 2012) were collected. Both have a spatial resolution of 1 km. The MODIS/NDVI is calculated using the atmospherically corrected reflectance and weighted temporal average of all 16-day composite products in the case of cloud-free or the maximum value in the case of clouds (Yang & Wang, 2011). The MODIS/albedo is derived using the 16-day anisotropy model provided in MODIS BRDF/Albedo Model Parameters product (MCD43B1), and it is an average of the underlying 500 m values (Yang & Wang, 2011).

### 3.3. Data preprocessing

All data were first projected to the Universal Transverse Mercator (datum: WGS-84, zone: North 50) and cropped into the study area. Then the least-cloud images (cloud cover <10%) were selected (Sun & Pinker, 2005; Weng, Lu, & Schubring, 2004; Zhou et al., 2011), because the cloud-contaminated pixels were invalid for our study. Furthermore, the water and high elevation (elevation >100 m) pixels were masked out using the modified normalized difference water index (Xu, 2005) and digital elevation model, respectively, because their temperatures were much lower than the simultaneous temperatures of the plain and low elevation land and they were not appropriate for the UHI analysis (Streutker, 2002).

## 4. Methodology

### 4.1. Centroid of the UHI

The urban growth in Beijing follows a concentric pattern (He et al., 2003) and the UHI in Beijing is appropriate for the one-core and symmetrical Gaussian distribution structure (Zhou et al., 2008). Thus, a Gaussian surface above rural background temperatures can be used to characterize its UHI continuously as follows (Streutker, 2002, 2003; Tran et al., 2006):

$$T(x, y) = T'(x, y) + a_0 \exp \left[ -\frac{((x-x_0) \cos\phi + (y-y_0) \sin\phi)^2}{2a_x^2} - \frac{((x-x_0) \sin\phi - (y-y_0) \cos\phi)^2}{2a_y^2} \right] \quad (1)$$

where  $(x, y)$  is the urban pixel location,  $T(x, y)$  and  $T'(x, y)$  are the surface temperature and background temperature, respectively,  $a_0$  is the magnitude,  $a_x$  and  $a_y$  are the half long and short axes of the Gaussian bottom ellipse, respectively,  $\phi$  is the orientation of the Gaussian surface, and  $(x_0, y_0)$  is the center of the Gaussian bottom ellipse.

The Gaussian volume of the UHI (Zhou et al., 2008) is defined as the space enclosed by the Gaussian surface, an elliptical cylinder with an identical Gaussian bottom ellipse and the background surface, as shown in Fig. 2. We define the geometric centroid of the Gaussian volume as the UHI centroid. Considering the symmetry of the Gaussian volume, its centroid is horizontally projected to  $(x_0, y_0)$ . Considering the Z-dimension of the centroid  $z_0$  is irrelevant with its horizontal location  $(x_0, y_0)$  and the orientation  $\phi$ , a simplified UHI Gaussian volume with the Gaussian surface function in Eq. (2) can be used to calculate  $z_0$  (Eq. (3)). The unit of the centroid  $(x_0, y_0, z_0)$  is ( $^{\circ}$ E,  $^{\circ}$ N,  $^{\circ}$ C), which represents (longitude, latitude, intensity).

$$z(x, y) = a_0 \exp \left[ -\frac{x^2}{2a_x^2} - \frac{y^2}{2a_y^2} \right] \quad (2)$$

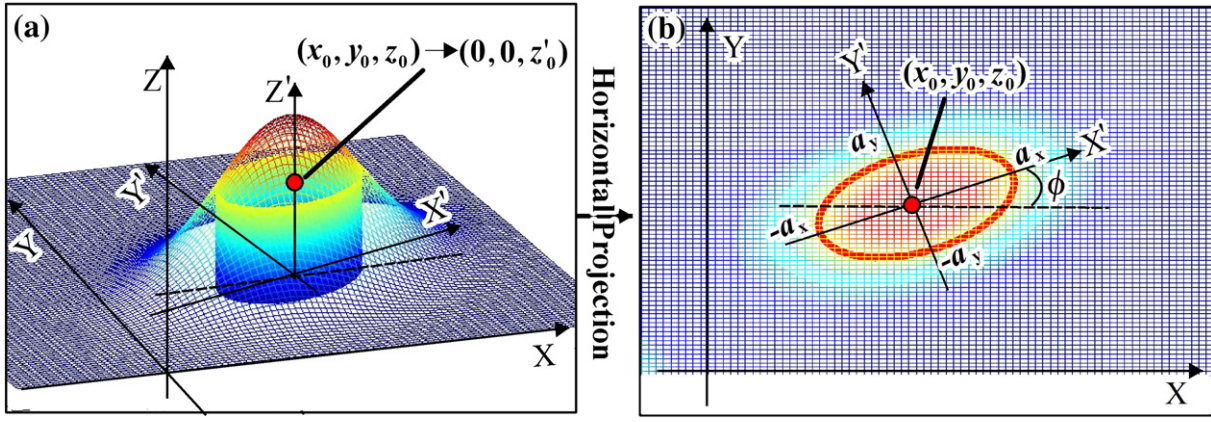


**Fig. 2.** Sketches of the Gaussian volume model. XYZ is the original coordinate system corresponding to Eq. (1), while X'Y'Z' is the transformed coordinate system corresponding to Eq. (2).

$$\begin{aligned}
 z_0 &= \frac{\iiint z \rho dv}{\iiint \Omega \rho dv} = \frac{\iint_D \left[ \int_0^{z(x,y)} zdz \right] d\sigma}{\iint_D \left[ \int_0^{z(x,y)} dz \right] d\sigma} = \frac{\int_{x_1}^{x_2} \left[ \int_{y_1(x)}^{y_2(x)} \left[ \frac{z^2}{2} \right]_0^{z(x,y)} dy \right] dx}{\int_{x_1}^{x_2} \left[ \int_{y_1(x)}^{y_2(x)} [z]_0^{z(x,y)} dy \right] dx} \\
 &= \frac{\frac{1}{2} \int_{-a_x}^{a_x} \left[ \int_{-a_y \sqrt{1-(x/a_x)^2}}^{a_y \sqrt{1-(x/a_x)^2}} (z(x,y))^2 dy \right] dx}{\int_{-a_x}^{a_x} \left[ \int_{-a_y \sqrt{1-(x/a_x)^2}}^{a_y \sqrt{1-(x/a_x)^2}} z(x,y) dy \right] dx}
 \end{aligned} \quad (3)$$

where  $\Omega$  is the bound closed space of the Gaussian volume,  $D$  is the footprint of the UHI and also the horizontal projection of the Gaussian volume, and  $\rho$  is the density of the Gaussian volume, which is regarded as a constant.

The background temperature  $T'(x,y)$  in this study adopted the mean rural LSTs instead of a tilt plane simulation of the rural LSTs as usual (Streutker, 2002, 2003; Tran et al., 2006), because after the high elevation pixels in the north and west of Beijing were eliminated, the valid rural pixels were mainly distributed in the east and south, and a tilt plane simulation would easily result in high northwestern and low southeastern background temperatures, and consequently, lead to a southeastern tendency of the UHI centroid.

#### 4.2. Centroids of the thermal landscape, NDVI and albedo

Many previous studies have investigated the effects of the land surface characteristics, atmospheric conditions, human activities and city structures on the UHI intensity (Gillies, Kustas, & Humes, 1997; Hafner & Kidder, 1999; Oke, 1987; Roth et al., 1989; Zhou, Chen, Zhang, & Zhan, 2013). Therefore, we only examined the relationship between the horizontal centroid locations of UHI and the thermal landscape, NDVI, and albedo.

The thermal landscape in the urban and rural areas was divided into five categories using mean-standard deviation (STD) method (Table 1) and their centroids were calculated according to Eq. (4).

$$x_{0i} = \frac{\sum_{x \in i} \sum_{y \in i} T(x,y)x}{\sum_{x \in i} \sum_{y \in i} T(x,y)}, \quad y_{0i} = \frac{\sum_{x \in i} \sum_{y \in i} T(x,y)y}{\sum_{x \in i} \sum_{y \in i} T(x,y)} \quad (4)$$

where  $(x_{0i}, y_{0i})$  is the centroid of the thermal category  $i$ , and other signatures have the identical meanings as shown in Eq. (1).

For NDVI data, the Gaussian volume model was applied to derive the NDVI centroid. For the albedo data that did not satisfy the Gaussian

assumption, a moving window was utilized in the urban area, and the central location of the window with a minimum average of albedo was treated as the albedo centroid.

## 5. Results

The Gaussian volume model was applied to all least-cloud LST images (around 19%, 14%, 33%, and 28% of all the daily images from 2000 to 2012 at four overpass times, respectively (Fig. 3a)), and the linear Pearson correlation coefficient  $r$  was calculated between the original UHI signal and the UHI signal predicted by Gaussian surface function for each image. Only the images with  $r > 0.5$  were regarded as well replicated by the Gaussian model and their results were regarded valid for further analysis (Fig. 3a). This contributed to filter the results that were significantly affected by the residual cloud (see Section 6.3). The 13-year or 11-year averaged monthly distributions (as percentage) of the valid results at four overpass times are shown in Fig. 3b.

The nighttime valid results, which were mostly distributed in February–May and September–November due to less precipitation and snow, exhibited a larger number compared to the daytime valid results. This was observed because the solar radiation enhances the instability of the atmospheric boundary and the difference of cooling rates between the urban and rural is maximized in the day (Hu & Brunsell, 2013), which causes an enhanced potential for cloud formation in the day, especially in the afternoon which leads to a smaller number at Aqua overpass time (~13:00 h). The lower nighttime LSTs compared to the simultaneous air temperatures make the nighttime boundary more stable. An inadequate number of daytime valid results were received during January–June and October–December. This was mostly induced by the less remarkable UHI in the day during these months, which did not fit the one-core and symmetrical Gaussian distribution. Consequently, we only focused on the daytime results during July–September. The time series of the valid results used in this study are displayed in Figs. 4 and 5. The impact of the missing data on the trajectory analysis of UHI centroid was discussed in Section 6.3.

**Table 1**

Thermal landscape classification using mean-standard deviation (STD) method, where  $T(x,y)$  is the surface temperature in location  $(x,y)$ , and  $m$  and  $std$  are the mean and STD of the LSTs in the urban and rural areas, respectively.

Thermal landscape category	Division
Hot	$T(x,y) \geq m + std$
Medium-hot	$m + std > T(x,y) \geq m + 0.5std$
Warm	$m + 0.5std > T(x,y) \geq m - 0.5std$
Medium-cold	$m - 0.5std > T(x,y) \geq m - std$
Cold	$T(x,y) < m - std$

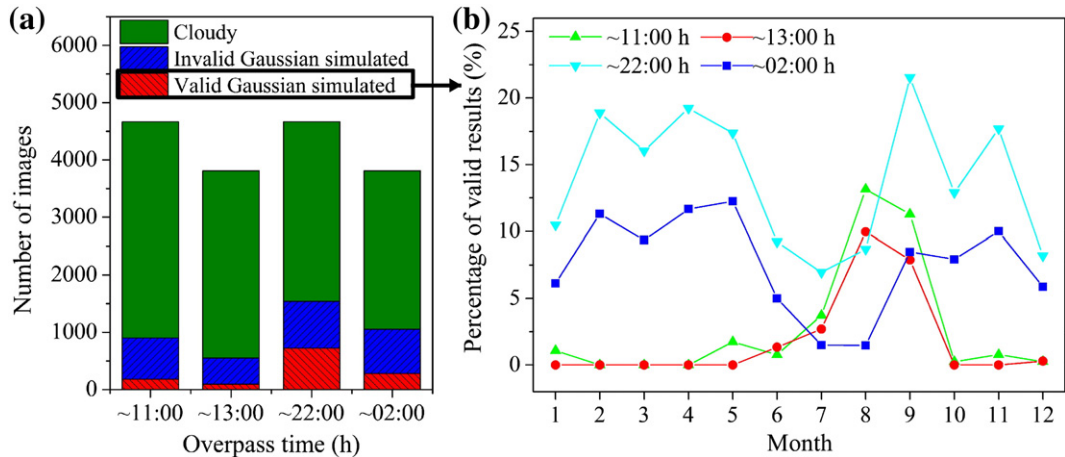


**Fig. 3.** Number of LST images at four overpass times. (a) The total number of cloudy (cloud cover > 10%), invalid (linear Pearson correlation coefficient  $r < 0.5$ ) and valid ( $r > 0.5$ ) Gaussian simulated LST images, and (b) the 13-year or 11-year averaged monthly distributions (as percentage) of the valid results, where the percentage is calculated as: total number of the valid results in a month / total number of all images in that month during 13 or 11 years.

### 5.1. Daily results

Considering the seasonal variation of the nighttime UHI centroid and its different temporal period (whole year) from that of the valid daytime centroid (in July–September), only the nighttime valid results in July–September were used for achieving day–night comparability, and the diurnal analysis is restricted to the period July–September. Table 2 shows the statistics of the valid daily results during 2000–2012. The core region of the UHI centroid is defined as a spheroid, where its centroid and radiiuses are represented by the mean and STDs in the three dimensions of UHI centroid, respectively. The horizontal projection map of their core regions is depicted in Fig. 6.

First, the mean centroids at the four times were mostly located in the Xicheng district near the city center and followed a diurnal trajectory similar to an '8' shape, where the daytime centroids were in the south of the nighttime ones. This was most likely attributed to the higher thermal inertia and shorter cooling rate of the north greenbelt. The mean intensity varied from 2.12 to 2.97 °C, with daytime intensity greater than nighttime one, and Aqua intensity greater than Terra one (0.31 °C and 0.03 °C higher during the day and night, respectively).

This may suggest that the Aqua visiting time in the day (~13:00 h) is better for observing the UHI compared to Terra (~11:00 h) because the difference between the thermal characteristics of the urban and rural land surfaces is more remarkable at that time.

Second, the daytime centroids exhibited higher STDs than the nighttime centroids, suggesting a stronger fluctuation during the day. This is reasonable considering the solar heating and more complex energy exchange between the surface and air during the day compared to during the night. Zhou et al. (2013) confirmed that the nighttime UHI is more stable than the daytime UHI. The core regions of the daytime centroids (38.57 and 34.88 km<sup>2</sup> for Terra and Aqua, respectively) were larger than the nighttime centroids (8.98 and 7.44 km<sup>2</sup> for Terra and Aqua, respectively). These regions are the primary thermal hazardous areas during the hot and wet summer seasons in Beijing, since the absolute urban surface temperatures are already very high.

Third, the dispersal in the latitude axis was larger than that in the longitude axis, which indicated that the UHI showed a more significant change in the north–south direction than in east–west direction during this period. This may be related to the variation of solar declination along latitude. Moreover, there was a considerable linear positive

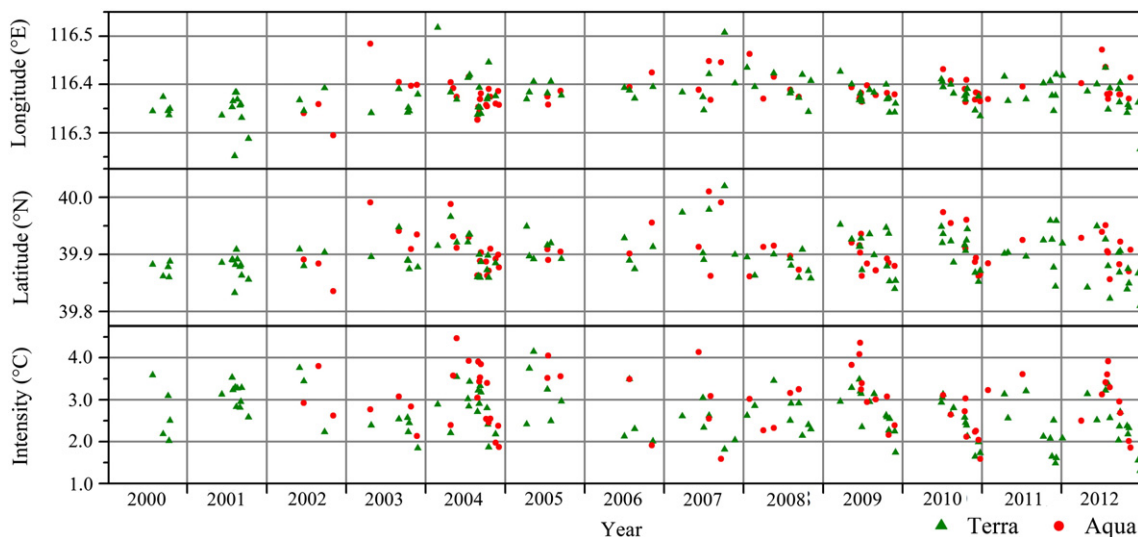


**Fig. 4.** Daily daytime UHI centroid in July–September from Terra and Aqua during 2000–2012. Each column represents the period from July 1st to September 31st.

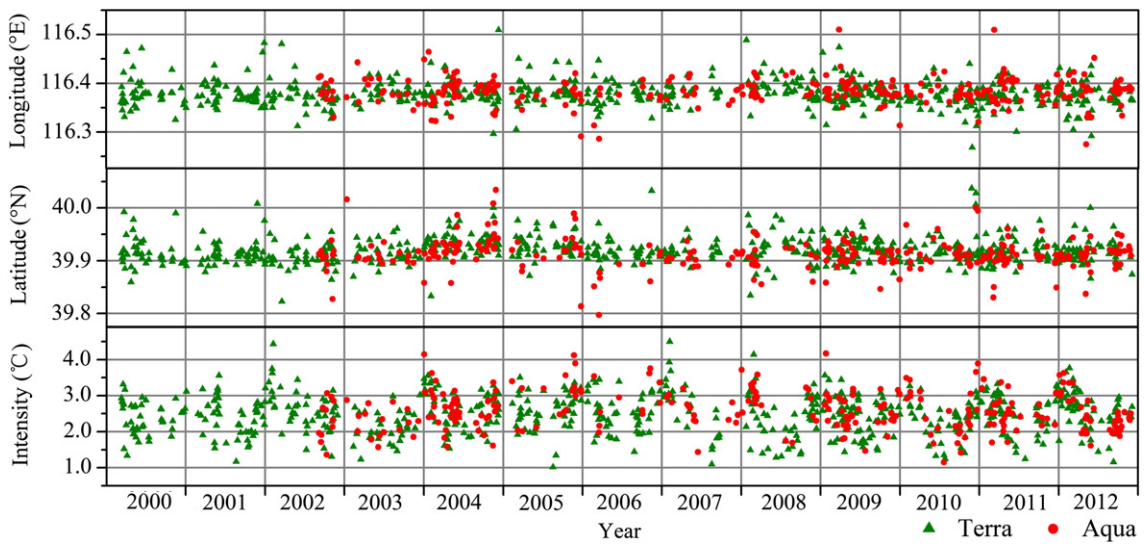


**Fig. 5.** Daily nighttime UHI centroid from Terra and Aqua during 2000–2012. Each column represents the period from January 1st to December 31st.

Pearson correlation coefficient (larger than 0.60) between the longitude and latitude of the daytime centroids, suggesting that the daytime centroids generally moved along the northeast–southwest direction.

## 5.2. Monthly results

To investigate the change patterns of UHI centroid on different temporal scales, we averaged the daily results to monthly results respectively for Terra and Aqua, as shown in Figs. 7 and 8. There were 23 daytime (70%) and 94 nighttime (75%) pairs that were comparable between Terra and Aqua monthly composite data, and their root mean square errors were (0.12 km, 0.12 km, 0.22 °C) during the daytime and (0.05 km, 0.07 km, 0.16 °C) during the nighttime. Because the differences were rather small on the monthly scale, the Terra and Aqua monthly composite datasets were further combined for increasing the valid data and simplifying the monthly variation analysis, as shown in Figs. 9 and 10, where the combined value maintained the single Terra or Aqua result when only Terra or Aqua was available. This mixture of combined and non-combined data had an insignificant impact on the monthly variation analysis (<85 m, <0.11 °C) due to the slight differences of longitude and latitude between Terra and Aqua (<170 m, 0.22 °C). Moreover, the monthly intensities from Terra and Aqua generally followed the same pattern of monthly variation, and therefore their combination would not distort the pattern. Overall, it was not necessary

to separately analyze the Terra and Aqua monthly dataset for the monthly pattern. Figs. 11 and 12 display the 13-year averaged Terra + Aqua monthly UHI centroids during the day and night.

The daytime UHI centroid moved by (1.85, 2.91) km in a northeast–southwest direction from July to September in the Dongcheng and Xicheng districts and the intensity varied from 2.16 to 3.09 °C, and peaked in August. The horizontal variation was more significant from July to August, while the variation of intensity was larger from August to September, revealing that the spatial distribution of the thermal energy rapidly changed in July and August, but the overall intensity remained stable in high values, and vice versa from August to September.

The nighttime centroid generally followed an anti-clockwise moving track (starting at the top from January to April, at the bottom from April to August, and at the right from August to December, respectively, similar to ‘ $\otimes$ ’ shape) throughout the year at the northwest corner of the city center. The intensity varied from 1.98 to 3.07 °C, with a valley appearing in July along with the highest STD and a peak appearing in January with the smallest STD. This may be attributed to the seasonal change of the difference between urban and rural cooling rates: the cooling rate of the urban surfaces is generally larger than the rural one in summer because of the numerous impervious surface in urban and the moist soil and vegetation in rural, but it is smaller in winter because of the increase of dry soil and the decay of vegetation in rural which increases the cooling rate. This reduces the difference between urban and

**Table 2**  
Statistics of the valid daily UHI centroids at four overpass times in July–September from 2000 to 2012. Lon, Lat and Int are short for longitude, latitude and intensity, respectively. Lon–Lat *r* represents the linear Pearson correlation coefficient between the longitude and latitude.

Time (h)	Centroid	Mean	STD	Max	Min	Range (Max–Min)	Core		Lon–Lat <i>r</i>	
							(Mean ± STD)			
~11:00	Lon (°E)	116.3777	0.0362	116.2520	116.5179	0.2659	116.3415–116.4139	0.61		
	Lat (°N)	39.8969	0.0354	39.8101	40.0196	0.2095	39.8615–39.9323			
	Int (°C)	2.66	0.57	1.30	4.15	2.85	2.09–3.23			
~13:00	Lon (°E)	116.3864	0.0319	116.2948	116.4844	0.1896	116.3545–116.4183	0.71		
	Lat (°N)	39.9056	0.0364	39.8355	40.0103	0.1748	39.8693–39.9420			
	Int (°C)	2.97	0.70	1.59	4.47	2.88	2.26–3.67			
~22:00	Lon (°E)	116.3800	0.0172	116.4440	116.3330	0.1111	116.3620–116.3970	0.15		
	Lat (°N)	39.9206	0.0172	39.9770	39.8820	0.0950	39.9034–39.9378			
	Int (°C)	2.12	0.47	3.17	1.02	2.16	1.64–2.59			
~02:00	Lon (°E)	116.3880	0.0174	116.4240	116.3620	0.0624	116.3710–116.4050	0.20		
	Lat (°N)	39.9145	0.0143	39.9505	39.8842	0.0663	39.9003–39.9288			
	Int (°C)	2.15	0.43	3.20	1.15	2.05	1.72–2.57			

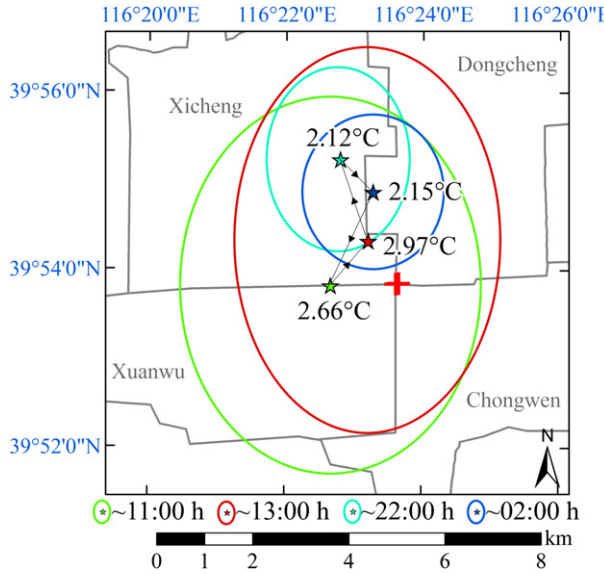


**Fig. 6.** The horizontal projection of the core regions of the UHI centroids at four overpass times. The ellipse and star represent the horizontal projection of the core area and the average centroid, respectively. The number near the star indicates the average Z-dimension of the UHI centroid. The background and red cross symbol refer to the administrative district boundaries and the city center of Beijing, respectively.

rural temperatures at summer night but enhances the difference at winter night. The fastest moving speed was found in November–December at (0.76 km, 0.86 km, 0.20 °C) in a month. This may partially result from the anthropogenic heat (such as urban heating supply), one of the major heat sources in winter (Offerle, Grimmond, Fortuniak, Klyszik, & Oke, 2006; Tong, Liu, Sang, & Hu, 2004; Zhou et al., 2013).

### 5.3. Annual results

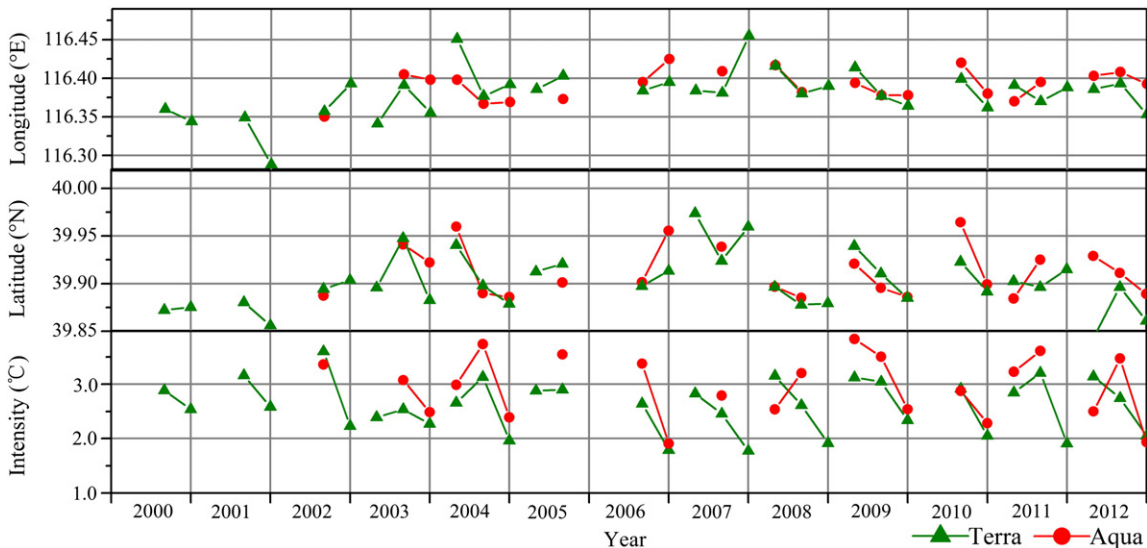
To investigate the inter-annual variation of UHI centroids, the Terra and Aqua monthly composite datasets were further aggregated to Terra and Aqua annual datasets, where the daytime set was formed using data from August only (excluding the data during July–September). This aggregation was performed because for daytime monthly results, (1) the annual distributions were different (Fig. 7), (2) the variation from July to September was significant (Figs. 11 and 12), (3) there were missing

monthly data during 2000–2012 in July and September but not in August (Fig. 7), and (4) the most significant UHI intensity appeared in August (Fig. 11).

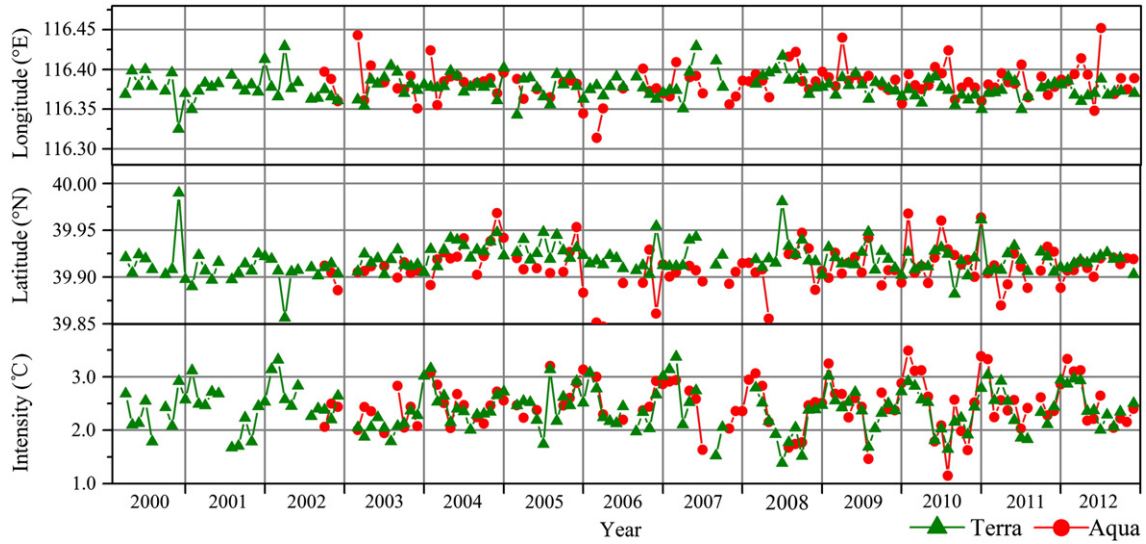
For nighttime annual results, the Terra and Aqua data were further combined, where the data in 2000 and 2001 were from Terra only. This combination did not affect the annual analysis significantly because of the slight difference between them as mentioned in Section 5.2. For daytime annual results in August, the average difference between Terra and Aqua during 2002–2012 was (0.03 km, 0.04 km, 0.43 °C). The differences in longitude and latitude were so small that they were further combined as the nighttime ones were, and this combination did not impact the inter-annual variation of the horizontal location. However, the difference of intensities was noticeable and thus combining the intensities from Terra and Aqua would cause an underestimation during 2000–2001 because Terra has lower intensity than Aqua (Section 5.1). Hence, the daytime intensities from Terra and Aqua were kept separately.

Fig. 13 shows the annual composite results during the day (in August) and night from 2000 to 2012. The daytime intensities in August from Terra and Aqua demonstrated a consistent annual variation: the intensity decreased from 2002 to 2003 and increased in 2004, and then kept decreasing until 2007 and then increasing until 2009, and finally fluctuated during 2010–2012. The nighttime intensity was relatively stable during 13 years. Table 3 lists their detailed inter-annual changing direction horizontally. Both Fig. 13 and Table 3 indicate that 2003 and 2007 are the most significant years in moving direction or speed changing of UHI centroid, and therefore the 13-year period was divided into three sub-periods: early period from 2000 to 2003, medium period from 2004 to 2007, and late period from 2008 to 2012.

The UHI centroids of the three sub-periods are displayed in Fig. 14. The daytime UHI centroid was located in Xuanwu district in the early period, and then moved northeast by (1.80, 1.31) km, remaining at the edge of the Forbidden City in the medium period. It then moved around 0.35 km to the east, staying inside the Forbidden City in the late period. Taken together, this revealed that the daytime centroid moved by (2.15, 1.31) km toward the northeast during 13 years. The nighttime UHI centroid was located just west of the Forbidden City and then moved by (0.43, 0.89) km to the northeast from the early to the late period. The movement of the UHI centroid from the early to medium period was more dramatic compared to the medium to late period. This was likely due to the numerous preparation projects prior to 2008 for the Beijing Olympic Games, such as the Green Olympics projects and the Olympic venues and facility constructions.



**Fig. 7.** Monthly averaged daytime UHI centroid from Terra and Aqua in July–September during 2000–2012. Each column represents the period from July to September.



**Fig. 8.** Monthly averaged nighttime UHI centroid from Terra and Aqua during 2000–2012. Each column represents the period from January to December.

## 6. Discussion

### 6.1. Relationship of the horizontal location of the UHI centroid with thermal landscape, NDVI and albedo

The centroids of five thermal landscape categories, NDVI and albedo were calculated (Section 4.2) using the cloud-least images. For NDVI, only those with linear Pearson correlation coefficient  $r > 0.5$  were regarded valid as it was for UHI (see Section 5). Consequently, the valid centroid of NDVI was only available in July–September, which may further confirm that the relationship between NDVI and LST is restricted in warm seasons (Quan, Zhan, Chen, & Liu, 2013; Yuan & Bauer, 2007; Zhan et al., 2012) because of the weak mitigation effect of vegetation in spring and winter (Zhou et al., 2013). In order to correlate the centroids of thermal landscape, NDVI and albedo with the UHI centroid on the same temporal scale, their Terra + Aqua monthly composite centroids were generated and compared in the same month. Fig. 15 shows the temporal variation of their horizontal location biases and Table 4 shows their average location biases and contribution rate C (Sun et al., 2010) to the variation of the UHI centroid.

First, the biases of the cold, medium-cold and warm thermal landscapes showed a large southeast deviation from the UHI centroid. This was because the geometric centroid of the thermal landscape was sensitive to the distribution of the pixels involved in computing, and the high northwestern but low southeastern terrain of Beijing resulted in that pixels with lower LSTs, which were mainly distributed in rural area, concentrated in the south and east, as previously mentioned in Section 4.1. Among the five thermal categories, the centroid of the hot landscape was the closest to the UHI centroid with mean biases of 2.4 km in the day and 2.92 km at night. This demonstrated that the horizontal location of the UHI centroid was highly relevant to the distribution of higher temperatures, which was also illustrated as hot island area by Zhang and Wang (2008).

The hot and medium-hot landscapes demonstrated strong positive contributions to the movement of the UHI centroid. The 2008 Olympic Games were held in the north of Beijing accompanied with plenty of new constructions built and commercial growth in the urban north, driving increasing thermal emission in the hot and medium-hot level. Moreover, the removal of Shougang Group, a steel producer, from Mentougou district reduced the western temperatures of Beijing, and

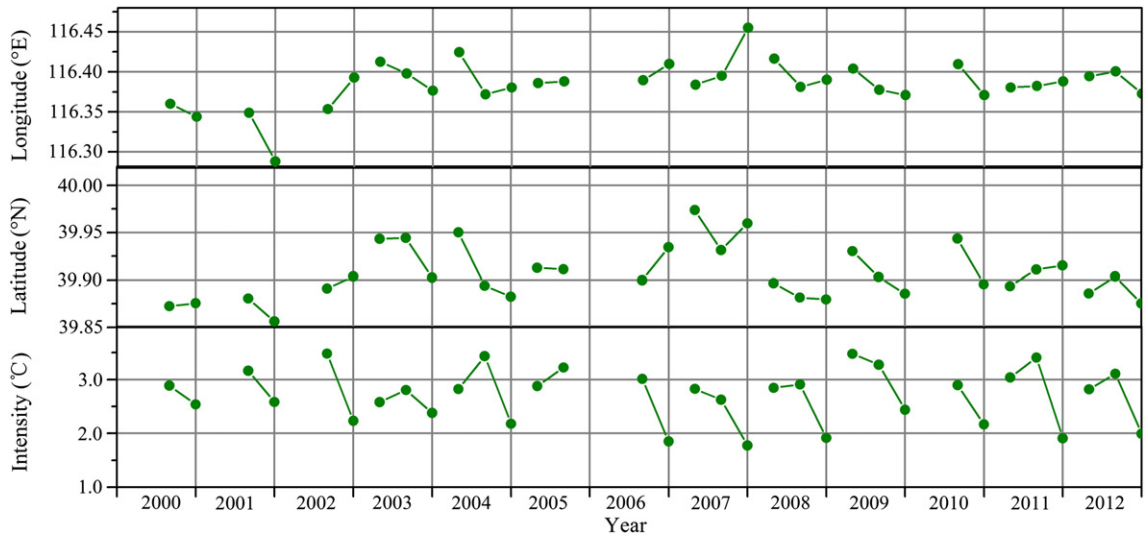


**Fig. 9.** Terra + Aqua monthly averaged daytime UHI centroid in July–September during 2000–2012. Each column represents the period from July to September.

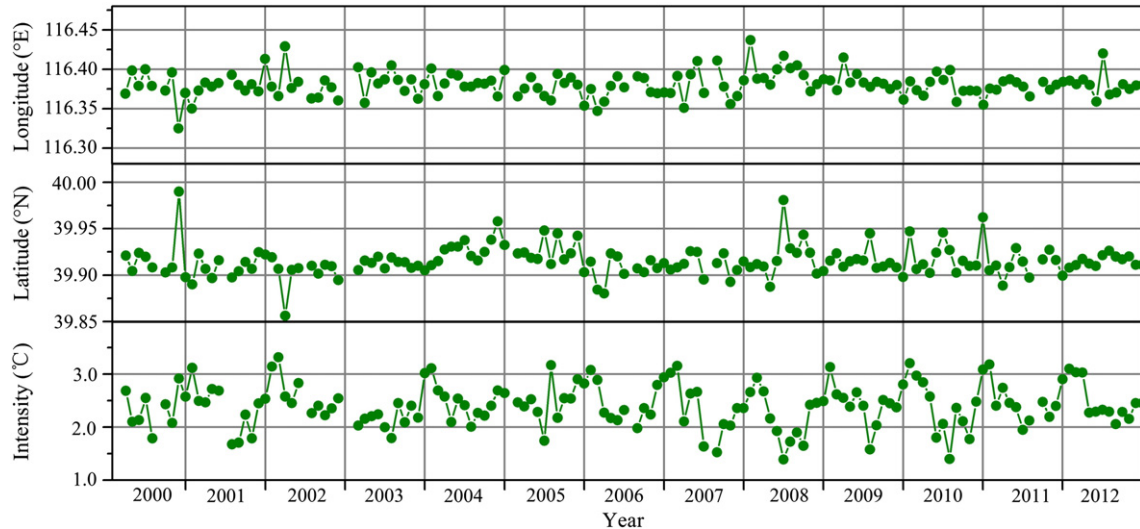


**Fig. 10.** Terra + Aqua monthly averaged nighttime UHI centroid during 2000–2012. Each column represents the period from January to December.

Tongzhou district, located at the east of the urban area, rapidly developed during these years. This was consistent with the northeast movement of the UHI centroid from 2000 to 2012. Importantly, the north region of Beijing is blocked by mountains and thus, the long-term urban development is considered toward the south instead of the north, with which the general movement of UHI centroid in long run might be consistent. In addition, the sum of the contributions of all five thermal landscapes was less than 100%. Therefore, the outer suburb or neighboring cities may also affect the UHI in Beijing.

Second, in summer, the centroids of NDVI were close to the UHI centroids with mean biases of 2.00 km in the day and 2.04 km at night. The distribution of the UHI was significantly correlated with the sink of vegetation coverage in the urban area for three main reasons: vegetation evapotranspiration enhances the latent heat flux from absorbed solar radiation (Grimmond & Oke, 1991), larger surface roughness of vegetation cover reduces the convective heat removal (Bonan, 1997), and heat storage of vegetation is low (Zhou et al., 2013). Its contribution to the variation of UHI centroid was positive in the day but negative at night, and the positive one was found to be

less than 10%, which might suggest more combined influence from other factors to the variation of the daytime UHI during this period.

Third, the albedo centroids were generally located in the northwest of the UHI centroids with biases of 5.23 km in the day and 5.56 km at night, which were much larger than that of NDVI. The difference between the Gaussian simulation of the UHI signals and minimum detection on the discrete albedo signals may be one of the major causes. Its contribution to the variation of the UHI centroid was positive at night but negative in the day, which contrasts with the NDVI. The city core area in Beijing exhibited a low albedo and high absorption due to dark impervious surfaces (including dark roofs and asphalt roads) and canyon geometric structures of the large numbers of old buildings, enabling them to obtain much shortwave radiation and store large amounts of heat during the daytime and then release high thermal energy at night (Jin, Kessomkiat, & Pereira, 2011; Zhou et al., 2013). Its positive

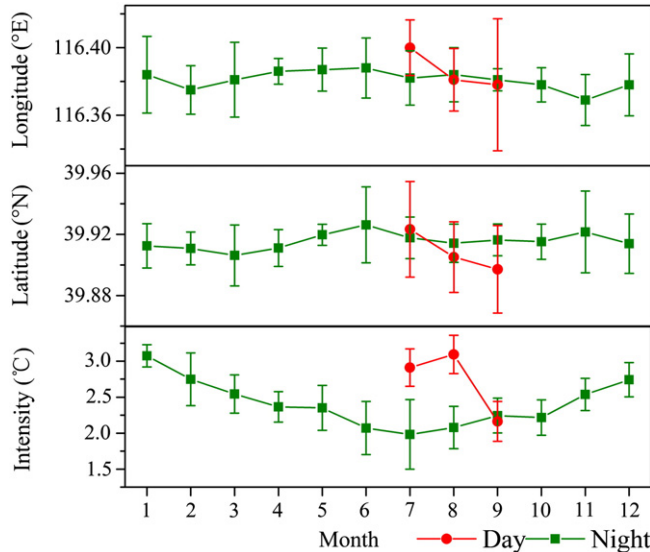


**Fig. 11.** 13-Year averaged Terra + Aqua monthly UHI centroids during the day and night. The error bar indicates the standard deviation within the month.

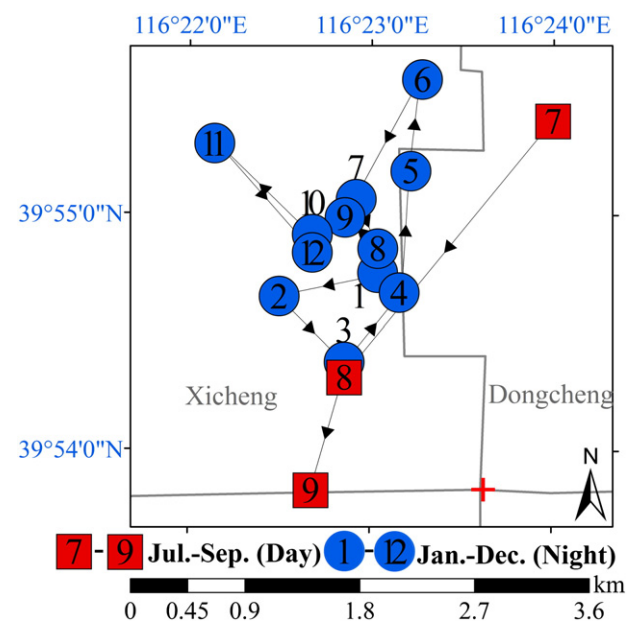


**Fig. 12.** The horizontal projection of the trajectories of 13-year averaged Terra + Aqua monthly UHI centroids during the day and night. The background and red cross symbol indicate the administrative district boundaries and the city center of Beijing, respectively.

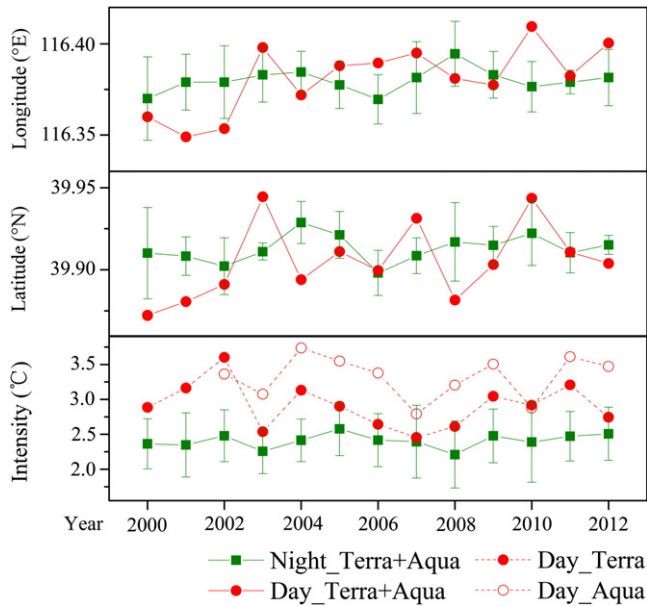


**Fig. 13.** Annual composite UHI centroids during the day (in August) and night from 2000 to 2012, where the longitude, latitude, and nighttime intensities are from the combination of Terra and Aqua annual composite data and the daytime intensities are from Terra and Aqua, respectively.

contribution was close to 50%, suggesting that the albedo was one of the primary factors dominating the variation of the nighttime UHI during this period.

Finally, the albedo change is usually related to the change of soil moisture, building canyons, vegetation abundance, impervious surface area, etc. (Jin et al., 2011). Considering the opposite contributions of NDVI and albedo, the contribution of albedo might be primarily attributed to the trapping of radiation by building canyons, and it may suggest that the urban buildings and vegetation had changed in the same direction, such as the Olympic sports center, Asian Games Village and Olympic park in the north of Chaoyang district. The effect of NDVI is stronger than the albedo in summer daytime (Zhou et al., 2013) but less remarkable at night (Zhan et al., 2013).

#### 6.2. Relationship between Z-dimension of UHI centroid and other UHI indicators

The Z-dimension of UHI centroid (Z) is a balance value separating the higher UHI intensities from the lower ones. It indicates the percentage of higher UHI intensities in the population. Larger Z demonstrates larger ratio of higher UHI intensities in the area. Theoretically speaking, Z increases with the Gaussian magnitude and it decreases with Gaussian extent. However, the effect of the Gaussian magnitude was much stronger than the effect of the Gaussian extent, and consequently Z was more correlated with the Gaussian magnitude than the extent.

**Table 3**

Detailed inter-annual horizontal moving direction of the UHI centroids during the day (in August) and night from 2000 to 2012.

Period	Day (August)	Period	Day (August)	Period	Night
2000–2001	↖	2007–2008	↙	2000–2004	↗
2001–2003	↗	2008–2009	↖	2004–2006	↗
2003–2004	↗	2009–2010	↗	2006–2008	↗
2004–2005	↗	2010–2011	↗	2008–2010	↖
2005–2006	↖	2011–2012	↖	2010–2012	↖
2006–2007	↗				

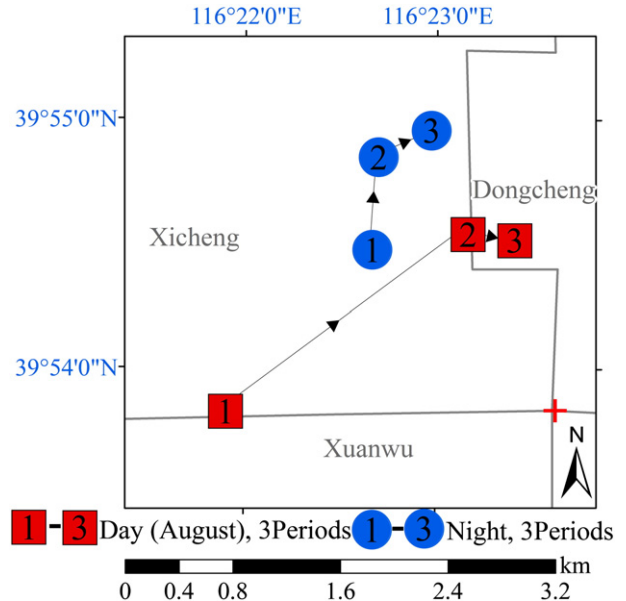


**Fig. 14.** The horizontal projection of the trajectories of the daytime (in August) and nighttime UHI centroids in the early (2000–2003), medium (2004–2007) and late (2008–2012) periods. The background and red cross symbol indicate the administrative district boundaries and the city center of Beijing, respectively.

The difference between urban and rural mean LSTs ( $D_{UR}$ ) is the most classical indicator for describing the surface UHI (Schwarz et al., 2011). The difference between Z and  $D_{UR}$  was investigated using the daily MODIS/LST dataset from 2000 to 2012, as shown in Fig. 16. Arranging all UHI intensities in the urban area from the lowest value to the highest value, then  $Z > D_{UR}$  indicates a left skewed distribution, and conversely,  $Z < D_{UR}$  indicates a right skewed distribution. Fig. 16 shows that Z is generally larger than  $D_{UR}$  during the day and night, which suggests that the peak of the distribution is in the right side of the population, indicating that the higher UHI intensities dominate the urban area. Moreover, their daytime difference decreased by year. This probably indicated that the domination of higher UHI intensities was weakened and the medium high UHI intensities were expanded during the period 2000–2012. For the nighttime, their difference showed a general seasonal pattern with a valley in the summer and a peak in the winter, the same as the seasonal variation of the nighttime Z. This might reveal that nighttime UHI generated higher spatial heterogeneity in the cold seasons than in the warm seasons. In addition, Z is more robust than  $D_{UR}$  because Z is more resistant to the outlier values and  $D_{UR}$  is more influenced by the discrimination of urban and rural areas. Wang et al. (2007) stated that different rural areas cause large differences of  $D_{UR}$ .

#### 6.3. Impact of missing data

More significant sensible heat flux, air turbulence, and convergence in urban area make it easier for clouds to form in urban compared to rural areas, especially during the daytime, which has obstructed the development of the UHI study using remote sensing for a long time (Morris, Simmonds, & Plummer, 2001). It forces researchers to select cloud-free images, to composite valid data, to retrieve LST under cloudy skies, or to apply cloud-interpolating algorithms. However, the cloud-free images are not always available for the specific study area or in the long term (Weng & Fu, 2014), and the composite data are related to the clouds (Hu & Brunsell, 2013). The retrieval of cloud contaminated LST (Jin, 2000; Lu, Venus, Skidmore, Wang, & Luo, 2011) or cloud interpolation of LST (Zhang et al., 2011) remains a challenge to meet rigid assumptions or to achieve a high precision. In this study, cloud-free

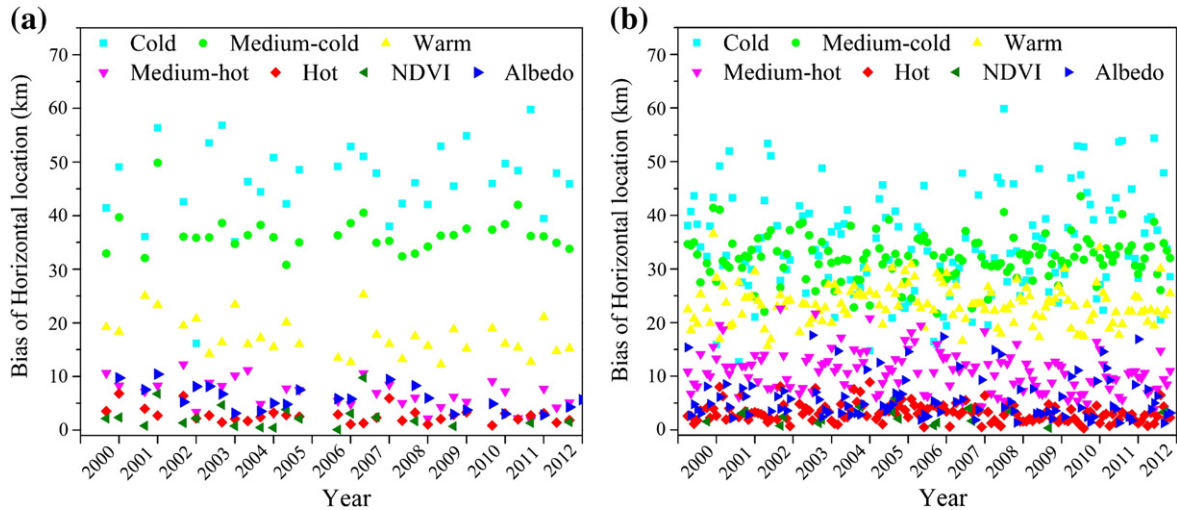


**Fig. 15.** Horizontal location biases between the UHI centroid and the centroids of the five thermal landscape categories, NDVI and albedo from 2000 to 2012. (a) The biases during the daytime from July to September each year. (b) The biases during the nighttime from January to December each year.

images were highly insufficient in the long term, and thereby a cloud coverage ratio of 90% was set as a threshold of clear skies.

To investigate the impact of missing data (no more than 10%) in each least-cloud LST image on the derived UHI centroid, we artificially added random or centralized clouds (less than 10% of the urban pixels) over the urban area originally under a clear sky. The biases between the UHI centroids of simulated cloudy images and the original clear ones are shown in Fig. 17. It illustrates that randomly distributed clouds have little influence on the centroid (biases less than 0.2 km and 0.3 °C), while the centralized clouds near the city center cause an underestimate of the UHI intensity. More clouds and a closer distance to the city center generate a larger bias, and the bias is considerable when the cloud cover ratio is higher than 4% and the distance to the city center is smaller than 20 km. At the worst condition, the biases reaches more than 13 km and –1.64 °C. Notice that this simulation is unable to take into account the residual cloud impact on the adjacent pixels (Hu & Brunsell, 2013).

There are 56, 30, 5, and 3 daily MODIS/LST images under the considerable cloudy condition aforementioned at four overpass times, respectively, and 88%, 97%, 100%, and 100% of them were excluded as invalid, respectively, based on the criterion used in this study: linear Pearson correlation coefficient  $r > 0.5$ . Although a few daytime images remained, this criterion is able to detect this type of error and help eliminate those results with large biases. Therefore, each valid daily result in this study was barely affected by the clouds near the city center.

However, the cloudy images caused large numbers of absent data in the time series of UHI centroid (Figs. 4 and 5), and it may bring biases to the temporal aggregation and thus the multi-temporal trajectory, where the uncertainty for the daytime centroid may be larger than that for the nighttime centroid because cloud patterns are more likely to form over urban areas during the daytime (Hu & Brunsell, 2013;

Romanov, 1999) and the fluctuation of daytime centroid is more significant (Section 5.1). Moreover, the relationship between the horizontal location of the daytime UHI centroid and NDVI (Section 6.1) may also be affected because the monthly composite MODIS/NDVI do not have missing data. To quantitatively illustrate this issue, we compared the average of the daily, monthly and annual composite UHI centroids from 2000 to 2012 as shown in Table 5, considering the average of the three datasets are the same in the case of no missing data, where Terra and Aqua were combined to show the mean impact (Hu & Brunsell, 2013).

During the daytime, the monthly composite dataset shows larger longitude and latitude but smaller intensity than the daily dataset, while the annual composite dataset shows smaller longitude and intensity but larger latitude. Both of them decrease the intensity because more daily results are in August when the highest UHI intensity appears (Fig. 3). Therefore, the diurnal variation of UHI centroid demonstrated in Section 5.1 may be slightly larger than that in reality. During the nighttime, both monthly and annual composite datasets show smaller longitude, latitude and intensity than the daily dataset, where the differences increase with the increase of temporal composite period. Therefore, the nighttime UHI centroid may show more significant monthly and annual changes in practice than those illustrated in Sections 5.2 and 5.3. However, the biases of horizontal location and intensity for both daytime and nighttime are no more than 0.63 km and 0.13 °C, respectively. Considering the spatial resolution (1 km) and accuracy (1.0 °C) of MODIS/LST, and compared to the multi-temporal variation of UHI centroid (Section 5) and the biases between NDVI and UHI centroids (Section 6.1), the impact of the missing data is considered negligible. It should be mentioned that this is not a common conclusion that can be applied on other UHI indicators or UHI with different features and variations.

**Table 4**

Average horizontal location biases and contribution rate C of the five thermal landscape categories, NDVI and albedo during the day (in July–September) and night from 2000 to 2012.

Mean location bias and contribution rate	Cold	Medium-cold	Warm	Medium-hot	Hot	NDVI	Albedo	
Day	Bias (km)	44.52	34.60	16.71	6.20	2.40	2.00	5.23
	C (%)	–189.98	–59.84	67.25	70.98	54.23	9.45	–14.08
Night	Bias (km)	32.91	30.52	22.38	10.57	2.92	2.04	5.56
	C (%)	–81.61	–21.44	–13.78	51.56	75.99	–30.92	45.55

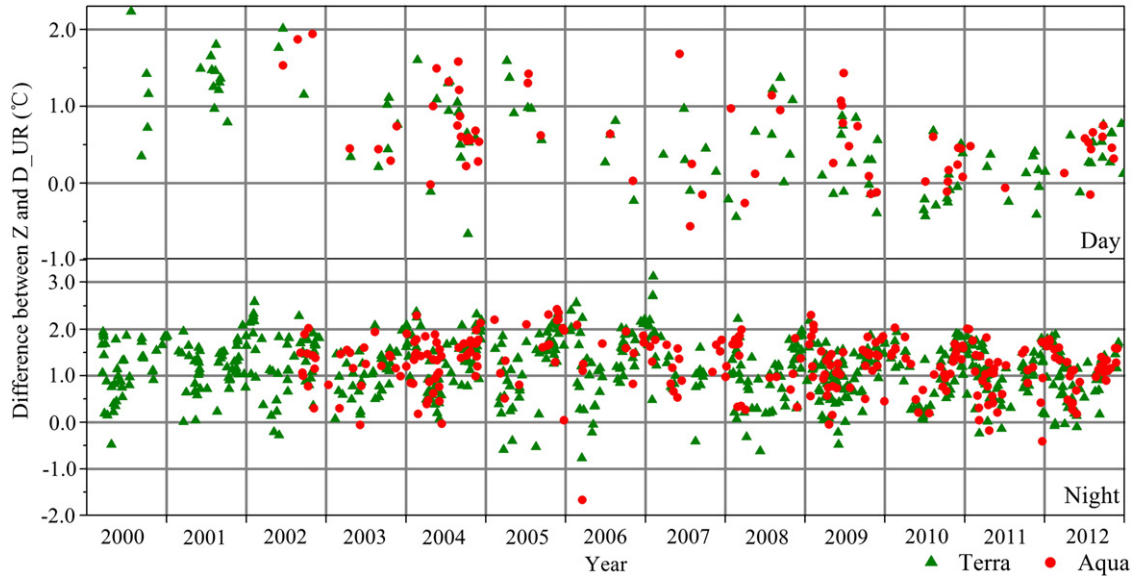


**Fig. 16.** Temporal variations of the difference between the Z-dimension of UHI centroid (Z) and the difference between mean urban and rural LSTs (D<sub>UR</sub>) from 2000 to 2012. Each column represents the period from July 1st to September 31st for the daytime and the period from January 1st to December 31st for the nighttime.

## 7. Conclusions

The centroid of the UHI is a comprehensive indicator used to evaluate the intensity and distribution characteristic of the UHI. The trajectory of UHI centroid provides insights for the spatio-temporal variation of the urban thermal environment. However, investigations of the trajectory of UHI centroid in three dimensions and on a multi-temporal scale are still rare. In this study, we used the Gaussian volume model to derive the centroid of UHI based on daily MODIS/LST products to

detect the diurnal, monthly and annual variations of the UHI in Beijing from 2000 to 2012.

On the diurnal scale during July–September, the UHI centroids were located in the Xicheng district near the city center at four MODIS overpass times, and the mean intensity varied from 2.12 to 2.97 °C. The daytime centroid was in the south of the nighttime centroid and has larger intensity and core area compared to the nighttime one, where Aqua obtains a higher intensity than Terra. The daytime centroid demonstrated a more dramatic variation than the nighttime one, and the north–south

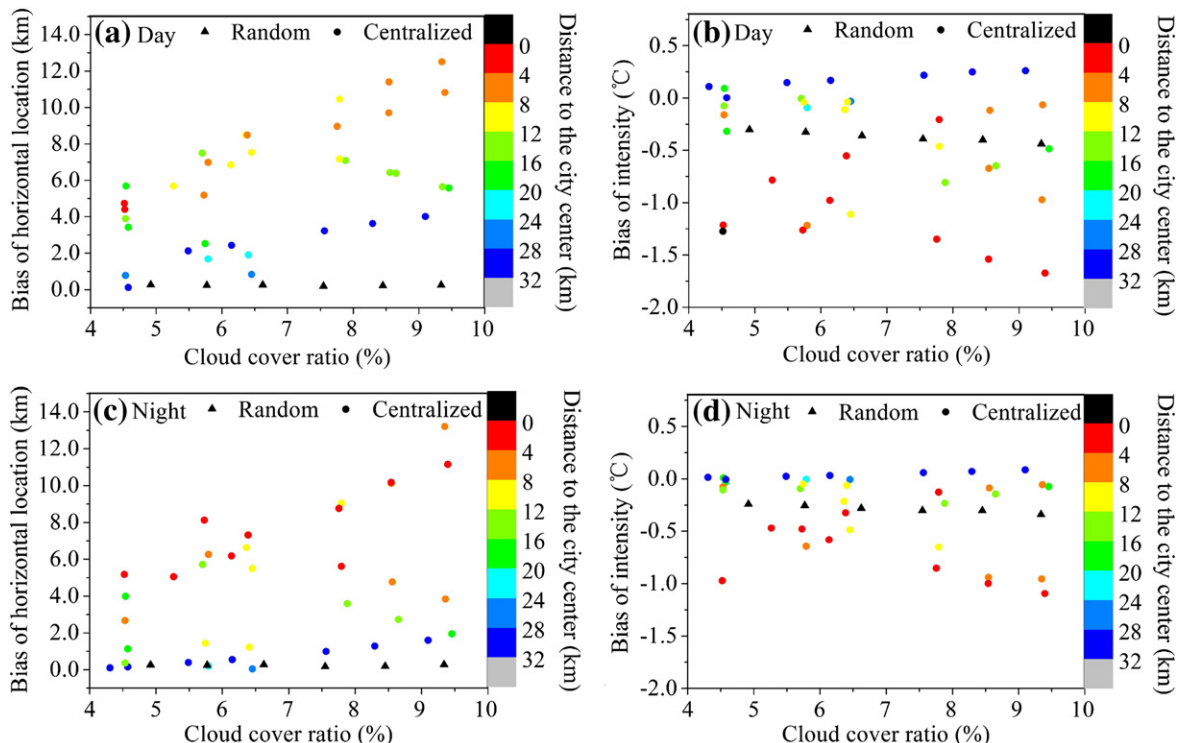


**Fig. 17.** The biases between the UHI centroids of simulated cloudy LST images and the original clear sky LST images during the day and night from Terra/MODIS acquired on August 12th, 2009. Random and centralized clouds were simulated.

**Table 5**

The average of the Terra + Aqua daily, monthly and annual composite UHI centroids from 2000 to 2012. Lon, Lat and Int are short for longitude, latitude and intensity, respectively, and Δ represents the difference between two datasets.

Time	Centroid	Daily	Monthly	Annual	ΔCentroid	Monthly–Daily	Annual–Daily
Day	Lon (°E)	116.3820	116.3848	116.3805	ΔLon (km)	0.24	−0.13
	Lat (°N)	39.9013	39.9066	39.9036	ΔLat (km)	0.59	0.26
	Int (°C)	2.81	2.71	2.73	ΔInt (°C)	−0.10	−0.08
Night	Lon (°E)	116.3810	116.3808	116.3799	ΔLon (km)	−0.02	−0.09
	Lat (°N)	39.9157	39.9154	39.9129	ΔLat (km)	−0.03	−0.30
	Int (°C)	2.54	2.41	2.41	ΔInt (°C)	−0.13	−0.13

direction indicated a more significant change in UHI compared to the east–west direction.

On the monthly scale, the daytime UHI centroid moved from the northeast to southwest by (1.85, 2.91) km from July to September in the Dongcheng and Xicheng districts and the intensity varied from 2.16 to 3.09 °C, where August received the highest intensity. The nighttime centroid generally followed an anti-clockwise moving track over 12 months at the northwest corner of the city center, and the intensity varied from 1.98 to 3.07 °C, where July showed the lowest intensity and the largest STD, while January demonstrated the highest intensity with the smallest variation range.

On the annual scale, the daytime UHI centroid in August and the nighttime UHI centroid moved toward the northeast by (2.15, 1.31) km and (0.43, 0.89) km, respectively. The daytime intensities in 2002, 2004, 2009 and 2011 are the most significant, while the nighttime intensities are relatively stable during 13 years. The change in the UHI centroid from 2000 to 2007 was more dramatic than that from 2008 to 2012, which was most likely due to the numerous preparation projects for the 2008 Beijing Olympic Games.

Moreover, the horizontal location of the UHI centroid was highly correlated with the distribution of high temperatures which showed positive contributions to the variation of UHI. The NDVI showed positive contributions, but less than 10%, to the variation of summer daytime UHI, while the albedo showed positive ones, close to 50%, to the movement of the nighttime UHI centroid, where the trapping of radiation by building canyons played a primary role. The temporal variations of the difference between Z and D\_UR demonstrated that the domination of higher UHI intensities was weakened and the medium high UHI intensities were expanded in the day from 2002 to 2012 and nighttime UHI generated higher spatial heterogeneity in the cold seasons than in the warm seasons. In addition, the impact of the missing data was found to be negligible in this study.

For the purpose of a multi-temporal variation study of the UHI centroid over a long period, we discarded the spatial resolution to pursue the higher temporal resolution. However, for observing the UHI at a district level, higher spatial resolution than 50 m is urgent (Sobrino, Oltra-Carrió, Sòria, Bianchi, & Paganini, 2012). In addition, the one-core Gaussian assumption may not be appropriate for the UHI in other cities or during other seasons except for summer in the daytime. Hence, future studies could put its interest in employing multi-centroid modeling at a high spatial resolution.

## Acknowledgments

This study was supported by grants obtained from the Project of Science & Technology for Beijing Excellent Doctoral Dissertation Instructor (grant no. 20131002702), New Century Excellent Talents in University (grant no. NCET-12-0057), State Key Laboratory of Earth Surface Processes and Resource Ecology (grant nos. 2013-ZY-09 and 2013-KF-01), and Natural Science Foundation of Jiangsu Province (grant no. BK20130566). We thank the anonymous reviewers for their insightful comments that helped us improve this paper.

## References

- Bonan, G. (1997). Effects of land use on the climate of the United States. *Climatic Change*, 37(3), 449–486.
- Chen, Y. H., Shi, P. J., & Li, X. B. (2002). Research on spatial thermal environment in Shanghai city based on remote sensing and GIS. *Acta Geodaetica et Cartographica Sinica*, 31(2), 139–144.
- Gallo, K. P., Tarpley, J. D., Mcnab, A. L., & Karl, T. R. (1995). Assessment of urban heat islands: A satellite perspective. *Atmospheric Research*, 37(1–3), 37–43.
- Gillies, R. R., Kustas, W. P., & Humes, K. S. (1997). A verification of the 'triangle' method for obtaining surface soil water content and energy fluxes from remote measurements of the normalized difference vegetation index (NDVI) and surface. *International Journal of Remote Sensing*, 18(15), 3145–3166.
- Grimmond, C. S. B., & Oke, T. R. (1991). An evapotranspiration-interception model for urban areas. *Water Resources Research*, 27(7), 1739–1755.
- Hafner, J., & Kidder, S. Q. (1999). Urban heat island modeling in conjunction with satellite-derived surface/soil parameters. *Journal of Applied Meteorology*, 38(4), 448–465.
- He, C. Y., Chen, J., Shi, P. J., & Fan, Y. D. (2003). City expansion model of metropolitan area in china: A case study of Beijing. *Acta Geographica Sinica*, 58(2), 294–304.
- Hu, L. Q., & Brunsell, N. A. (2013). The impact of temporal aggregation of land surface temperature data for surface urban heat island (SUHI) monitoring. *Remote Sensing of Environment*, 134, 162–174.
- Hu, L. Q., Brunsell, N. A., Monaghan, A. J., Barlage, M., & Wilhelmi, O. V. (2014). How can we use MODIS land surface temperature to validate long-term urban model simulations? *Journal of Geophysical Research, [Atmospheres]*, <http://dx.doi.org/10.1002/2013JD021101>.
- Imhoff, M. L., Zhang, P., Wolfe, R. E., & Bounoua, L. (2010). Remote sensing of the urban heat island effect across biomes in the continental USA. *Remote Sensing of Environment*, 114(3), 504–513.
- Jin, M. (2000). Interpolation of surface radiative temperature measured from polar orbiting satellites to a diurnal cycle: 2. Cloudy-pixel treatment. *Journal of Geophysical Research, [Atmospheres]*, 105(D3), 4061–4076.
- Jin, M. S., Kessomkiat, W., & Pereira, G. (2011). Satellite-observed urbanization characters in Shanghai, China: Aerosols, urban heat island effect, and land-atmosphere interactions. *Remote Sensing*, 3(1), 83–99.
- Konopacki, S., & Akbari, H. (2002). Energy savings for heat-island reduction strategies in Chicago and Houston (including updates for Baton Rouge, Sacramento, and Salt Lake City). Draft final report. Berkeley: University of California (LBNL-49638).
- Lu, L., Venus, V., Skidmore, A., Wang, T., & Luo, G. (2011). Estimating land-surface temperature under clouds using MSG/SEVIRI observations. *International Journal of Applied Earth Observation and Geoinformation*, 13(2), 265–276.
- Morris, C. J. G., Simmonds, I., & Plummer, N. (2001). Quantification of the influences of wind and cloud on the nocturnal urban heat island of a large city. *Journal of Applied Meteorology*, 40(2), 169–182.
- Offerle, B., Grimmond, C. S. B., Fortuniak, K., Khsik, K., & Oke, T. R. (2006). Temporal variations in heat fluxes over a central European city centre, 84(1–3), 103–115.
- Oke, T. R. (1987). *Boundary layer climates* (2nd ed.). London: Methuen.
- Patz, J. A., Campbell-Lendrum, D., Holloway, T., & Foley, J. A. (2005). Impact of regional climate change on human health. *Nature*, 438(7066), 310–317.
- Quan, J. L., Zhan, W. F., Chen, Y. H., & Liu, W. Y. (2013). Downscaling remotely sensed land surface temperatures: A comparison of typical methods. *International Journal of Remote Sensing*, 2, 374–387.
- Rajasekar, U., & Weng, Q. (2009). Urban heat island monitoring and analysis using a non-parametric model: A case study of Indianapolis. *ISPRS Journal of Photogrammetry and Remote Sensing*, 64(1), 86–96.
- Rizwan, A. M., Dennis, L. Y. C., & Liu, C. (2008). A review on the generation, determination and mitigation of urban heat island. *Journal of Environmental Sciences*, 20(1), 120–128.
- Romanov, P. (1999). Urban influence on cloud cover estimated from satellite data. *Atmospheric Environment*, 33(24–25), 4163–4172.
- Roth, M., Oke, T. R., & Emery, W. J. (1989). Satellite-derived urban heat islands from three coastal cities and the utilization of such data in urban climatology. *International Journal of Remote Sensing*, 10(11), 1699–1720.
- Schwarz, N., Lautenbach, S., & Seppelt, R. (2011). Exploring indicators for quantifying surface urban heat islands of European cities with MODIS land surface temperatures. *Remote Sensing of Environment*, 115(12), 3175–3186.
- Sobrino, J. A., Oltra-Carrió, R., Sòria, G., Bianchi, R., & Paganini, M. (2012). Impact of spatial resolution and satellite overpass time on evaluation of the surface urban heat island effects. *Remote Sensing of Environment*, 117, 50–56.

- Song, Y. L., & Zhang, S. Y. (2003). The study on heat island effect in Beijing during last 40 years. *Chinese Journal of Eco-Agriculture*, 11(4), 126–129.
- Stewart, I. D. (2011). A systematic review and scientific critique of methodology in modern urban heat island literature. *International Journal of Climatology*, 31(2), 200–217.
- Streutker, D. R. (2002). A remote sensing study of the urban heat island of Houston, Texas. *International Journal of Remote Sensing*, 23(13), 2595–2608.
- Streutker, D. R. (2003). Satellite-measured growth of the urban heat island of Houston, Texas. *Remote Sensing of Environment*, 85(3), 282–289.
- Sun, D., & Pinker, R. T. (2005). Implementation of GOES-based land surface temperature diurnal cycle to AVHRR. *International Journal of Remote Sensing*, 26(18), 3975–3984.
- Sun, Q. Q., Wu, Z. F., & Tan, J. J. (2010). Spatio-temporal changes of urban thermal environment with thermal centroid in Guangzhou. *Scientia Geographica Sinica*, 30(4), 620–623.
- Tong, H., Liu, H. Z., Sang, J. G., & Hu, F. (2004). The impact of urban anthropogenic heat on Beijing heat environment. *Climatic and Environmental Research*, 9(3), 409–421.
- Tran, H., Uchihama, D., Ochi, S., & Yasuoka, Y. (2006). Assessment with satellite data of the urban heat island effects in Asian mega cities. *International Journal of Applied Earth Observation and Geoinformation*, 8(1), 34–48.
- Voogt, J. A., & Oke, T. R. (2003). Thermal remote sensing of urban climates. *Remote Sensing of Environment*, 86(3), 370–384.
- Wan, Z. M. (2008). New refinements and validation of the MODIS land-surface temperature/emissivity products. *Remote Sensing of Environment*, 112(1), 59–74.
- Wan, Z. M., & Dozier, J. (1996). A generalized split-window algorithm for retrieving land-surface temperature from space. *IEEE Transactions on Geoscience and Remote Sensing*, 34(4), 892–905.
- Wan, Z. M., Zhang, Y. L., Zhang, Q. C., & Li, Z. L. (2002). Validation of the land-surface temperature products retrieved from Terra Moderate Resolution Imaging Spectroradiometer data. *Remote Sensing of Environment*, 83(1–2), 163–180.
- Wang, T. X., Chen, S. L., & Yan, G. J. (2009). Estimation of land surface parameters and spatio-temporal characteristics of urban heat island. *Scientia Geographica Sinica*, 29(5), 697–702.
- Wang, Y., & Hu, F. (2006). Variations of the urban heat island in summer of the recent 10 years over Beijing and its environment effect. *Chinese Journal of Geophysics*, 49(1), 61–68.
- Wang, J. K., Wang, K. C., & Wang, P. C. (2007). Urban heat (or cool) island over Beijing from MODIS land surface temperature. *International Journal of Remote Sensing*, 28(3), 330–339.
- Weng, Q. H., & Fu, P. (2014). Modeling annual parameters of clear-sky land surface temperature variations and evaluating the impact of cloud cover using time series of Landsat TIR data. *Remote Sensing of Environment*, 140, 267–278.
- Weng, Q. H., Lu, D. S., & Schubring, J. (2004). Estimation of land surface temperature-vegetation abundance relationship for urban heat island studies. *Remote Sensing of Environment*, 89(4), 467–483.
- Weng, Q. H., & Quattrochi, D. A. (2006). Thermal remote sensing of urban areas: An introduction to the special issue. *Remote Sensing of Environment*, 104(2), 119–122.
- Xie, M. M., Fu, M. C., & Wang, Y. L. (2011). Changing trajectory of urban heat islands in Shenzhen, China. *Remote Sensing, Environment and Transportation Engineering (RSETE)*, 2011 International Conference (pp. 164–167).
- Xu, H. Q. (2005). A study on information extraction of water body with the Modified Normalized Difference Water Index (MNDWI). *International Journal of Remote Sensing*, 9(5), 589–595.
- Yang, J. X., & Wang, Y. P. (2011). Estimating evapotranspiration fraction by modeling two-dimensional space of NDVI/albedo and day–night land surface temperature difference: A comparative study. *Advances in Water Resources*, 34(4), 512–518.
- Yuan, F., & Bauer, M. E. (2007). Comparison of impervious surface area and normalized difference vegetation index as indicators of surface urban heat island effects in Landsat imagery. *Remote Sensing of Environment*, 106(3), 375–386.
- Zhan, W. F., Chen, Y. H., Wang, J. F., Zhou, J., Quan, J. L., Liu, W. Y., et al. (2012). Downscaling land surface temperatures with multi-spectral and multi-resolution images. *International Journal of Applied Earth Observation and Geoinformation*, 18, 23–36.
- Zhan, W. F., Chen, Y. H., Zhou, J., & Li, J. (2011). Spatial simulation of urban heat island intensity based on the Support Vector Machine technique: A case study in Beijing. *Acta Geodaetica et Cartographica Sinica*, 40(1), 96–103.
- Zhan, W. F., Chen, Y. H., Zhou, J., Wang, J. F., Liu, W. Y., Voogt, J., et al. (2013). Disaggregation of remotely sensed land surface temperature: Literature survey, taxonomy, issues, and caveats. *Remote Sensing of Environment*, 131, 119–139.
- Zhang, J. H., Hou, Y. Y., Li, G. C., Yan, H., & Yang, L. M. (2005). The research of the satellite sensing and the influence factor over Beijing and its surrounding zones. *Science China*, 35D, 187–194.
- Zhang, J., Qin, Z. H., Liu, M., Tu, L. L., Zhou, Y., & Yang, Q. (2011). Estimating of land surface temperature under the cloud cover with spatial interpolation. *Geography and Geo-Information Science*, 27(6), 45–49.
- Zhang, J. Q., & Wang, Y. P. (2008). Study of the relationships between the spatial extent of surface urban heat islands and urban characteristic factors based on Landsat ETM+ data. *Sensors*, 8(11), 7453–7468.
- Zhou, J., Chen, Y. H., Li, J., Weng, Q. H., & Yi, W. B. (2008). A volume model for urban heat island based on remote sensing imagery and its application: A case study in Beijing. *International Journal of Remote Sensing*, 29(5), 734–742.
- Zhou, J., Chen, Y. H., Wang, J. F., & Zhan, W. F. (2011). Maximum nighttime urban heat island (UHI) intensity simulation by integrating remotely sensed data and meteorological observations. *IEEE Journal of Selected Topics in Applied Earth Observations and Remote Sensing*, 4(1), 138–146.
- Zhou, J., Chen, Y. H., Zhang, X., & Zhan, W. F. (2013). Modeling the diurnal variations of urban heat islands with multi-source satellite data. *International Journal of Remote Sensing*, 34(21), 7568–7588.